

rh-In₂O₃ Nanoparticles for Efficient Photocatalytic Degradation of Rifampin

Shunxi Tang, Xinyou Zhang, Shufeng Li, Chupei Zheng, Huili Li, and Xianbo Xiao*



Cite This: *ACS Omega* 2023, 8, 40099–40109



Read Online

ACCESS |



Metrics & More

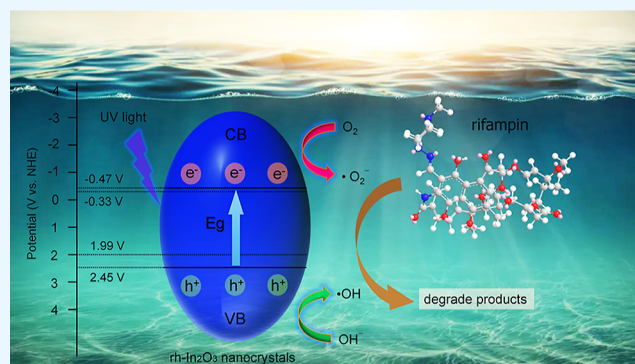


Article Recommendations



Supporting Information

ABSTRACT: Photodegradation, a widely accepted and promising technology, has gained significant attention for addressing the escalating concerns of environmental deterioration. In this article, rhombohedral corundum-type In₂O₃ nanocrystals were obtained from the transformation of InOOH via a simple calcining process. Under ultraviolet light irradiation, they showed higher photocatalytic activity in the decomposition of rifampin compared to that of the cubic phase In₂O₃ and P25–TiO₂. Furthermore, the probable pathway and the feasible mechanism for the degradation of rifampin were also deeply explored and discussed.



INTRODUCTION

Over the past few decades, antibiotics have gained widespread recognition as remarkable agents for combating various bacterial infections. Rifampin, as a broad-spectrum antimicrobial, is commonly used to treat meningococcal carriers and tuberculosis and even in animal husbandry and aquaculture.¹ Unfortunately, due to the excessive or improper use and incomplete metabolism in the body, part of the used rifampin remains active after excretion and then is released into the environment. Because of the stable chemical structure and hydrophobic property of rifampin, it will widely accumulate in aquatic resources, resist biological degradation, and finally get into the human food chain.² As we know, frequent intake of antibiotics may lead to the development of human drug resistance, increase the risk of intestinal dysbacteriosis, and even cause potentially severe medical problems.¹ Currently, antibiotics are perceived as emerging contaminants in the ecological environment, and they have attracted significant attention. Thus, in order to solve the ecological crisis and human health risk, a cost-effective approach is urgently required for the removal of rifampin (RIF) from wastewater. In recent years, a variety of methods have been used, mainly including physical adsorption, biodegradation, advanced oxidation technologies (such as photocatalysis, sonocatalysis, Fenton, and ozonation), and so forth, for removing varieties of antibiotic pollutants.^{3–9} However, conventional physical and biological treatment methods have shown limitations in terms of sorption affinity, microbial dissipation, and degradation rates, resulting in the persistence of these recalcitrant antibiotics in the environment.² In contrast, semiconductor-based photocatalysis has been proven to be a promising

technology and widely used to decrease the negative environmental impacts of these harmful antibiotics and other hazardous wastes in aqueous media.^{7,8,10–13}

With the development of nanofabrication techniques, a variety of inorganic metal oxide semiconductor nanostructures have been prepared and considered to be favorable photocatalysts for their large surface area, excellent adsorption, and satisfactory photochemical stability.^{14–16} Among them, indium oxide (In₂O₃) has received substantial attention since it has excellent photocatalytic performances and outstanding optical properties.^{17,18} In₂O₃ usually crystallizes in the stable cubic phase (c-In₂O₃) at ambient conditions, whereas the metastable rhombohedral corundum-type phase (rh-In₂O₃) is under high temperature and pressure conditions (Table S1).^{19–21} For c-In₂O₃, numerous morphologies, different synthesis processes, and their applications in various fields have been extensively and deeply researched in recent years.^{22–24} In contrast, due to the extreme reaction conditions, the syntheses and properties of rh-In₂O₃ nanostructures have been seldom reported. Previous studies have demonstrated that some of the prepared rh-In₂O₃ nanostructures exhibited superior photoelectric and gas sensing properties.^{25–29} However, only limited research suggested that rh-In₂O₃ should be an efficient photocatalyst for the degradation of environmental pollutants. For instance, Yin

Received: April 18, 2023

Accepted: October 2, 2023

Published: October 17, 2023



and Cao fabricated the hollow rh-In₂O₃ nanocrystals to photodegrade rhodamine B and methylene blue under ultraviolet (UV) light.³⁰ Wu et al. and Zhou et al. found that the porous flowerlike and urchin-like rh-In₂O₃ should be better candidates for the degradation of tetracycline and oxytetracycline, respectively.^{31,32} Yet, as far as we know, it is rare to have a report on the utilization of rh-In₂O₃ nanostructures as efficient photocatalysts for the photodegradation of rifampin.

Herein, we present the transformation from ultrathin InOOH nanowires to rh-In₂O₃ and c-In₂O₃ nanocrystals via a simple calcining process. Their morphological characteristics and optical and photoelectrical properties were carefully checked. Furthermore, the photocatalytic activities of rh-In₂O₃ were evaluated by degrading rifampin under UV light irradiation with c-In₂O₃ and P25-TiO₂ nanocrystals for comparison. Additionally, the probable pathway and feasible mechanism for degradation were comprehensively discussed.

EXPERIMENTAL SECTION

Synthesis of rh-In₂O₃ and c-In₂O₃ Nanocrystals. Fine powders of InOOH nanowires used as precursors in our experiments were prepared following the steps described in the previous work (Figure S1).³³ A quartz crucible containing 0.3 g of InOOH powders was placed in a muffle furnace and heated to various temperatures (200, 300, 400, 500, 600, and 700 °C) at a heating ramp rate of 5 °C/min under an air atmosphere. After maintaining each desired temperature for 5 h, the crucible was allowed to cool naturally to room temperature, resulting in the formation of white target products for further characterization.

Materials Characterization. The crystalline phases of the products annealed at different temperatures were determined by using a Bruker D8 ADVANCE powder X-ray diffractometer equipped with Cu K α radiation. Further analyses of these ray diffraction (XRD) data were performed with Rietveld refinements using GSAS-II software.^{34,35} Their morphologies were imaged with a field emission scanning electron microscope (JSM 7001F). Further structural information and elemental distributions were analyzed by a JEM-2200FS transmission electron microscope coupled to an energy-dispersive spectrometer. Additionally, X-ray photoelectron spectroscopy (XPS, Thermo ESCALAB 250Xi) was employed to determine the elemental compositions, chemical states, and valence band values of the samples. In order to show the optical properties of these samples, ultraviolet–visible (UV–vis) absorption spectra were examined by using a Shimadzu UV-3150 spectrometer. The specific surface areas and pore size distribution were observed on an ASAP 2020 analyzer (using Brunauer–Emmett–Teller and Barrett–Joyner–Halenda models). All of the electron spin resonance (ESR) spectra were recorded by a JEOL JES-FA200 spectrometer at room temperature.

Photoelectrochemical Measurements. The photoelectrochemical performances, such as the Nyquist plots, transient photocurrent–time ($I-t$) curves, and Mott–Schottky ($M-S$) plots, were evaluated on a Chenhua CHI660E electrochemical workstation with a standard three-electrode system. The ITO glass covered with the catalyst, Pt wire, Ag/AgCl (saturated KCl), and 0.1 M Na₂SO₄ solution were utilized as the working electrode, counter electrode, reference electrode, and electrolyte, respectively. In addition, a 300 W Xe lamp was used as the light source.

Photocatalytic Activity Test. The photocatalytic activities of the as-prepared rh-In₂O₃, c-In₂O₃, and commercial P25-TiO₂ nanocrystals were evaluated by the degradation of RIF under UV irradiation in a photocatalytic reactor (Figure S2 and Table S2). Parallel experiments were conducted, with 25 mg of the catalyst mixed into a 10 mg/L RIF solution (250 mL) for each group. Then, these solutions were transferred to darkness under continuous stirring for establishing sorption equilibrium. 1 hour later, they were allowed to expose to UV light for up to 120 min (magnetically stirred, 25 °C). During this process, 5 mL of the RIF solution was taken out from one of the groups in turn at regular intervals for analyzing the variations of the RIF solution concentrations (using a Shimadzu UV-2600 spectrophotometer). Finally, the possible intermediates of RIF generated during the photocatalytic degradation processes were characterized using ultrahigh-performance liquid chromatography coupled to high-resolution mass spectrometry (UHPLC-HRMS). Chromatographic separation was performed on an UltiMate 3000 liquid chromatograph with a Hypersil GOLD C18 column (2.1 \times 100 mm, 3 μ m). The column temperature and flow rate were maintained at 25 °C and 0.25 mL/min, respectively. The mobile phase was composed of methanol (A) and 0.1% formic acid (B). The gradient elution conditions were set as follows: 0–2 min (5% A), 2–15 min (5–90% B), 15–20 min (90% A), 20–21 min (90–5% A), and 21–27 min (5% A). Mass spectra (MS) were acquired by using a Thermo Q-Exactive mass spectrometer equipped with a heated electrospray ionization source. The spray voltage was set at 3.2 kV for the positive mode and 3.5 kV for the negative mode, and the resolutions of the full MS and data-dependent MS² (dd-MS²) scan modes were 70,000 and 17,500, respectively.

RESULTS AND DISCUSSION

Characterization of rh-In₂O₃ Nanocrystals. The calcination of the InOOH nanowires was carefully investigated by a series of time-dependent experiments. The corresponding XRD analysis and SEM observation are shown in Figures S3 and S4 for details. It is clear that these InOOH nanowires undergo a transition to the rh-In₂O₃ and c-In₂O₃ nanocrystals successively with increasing temperature. From Figure 1a, XRD examination indicates that the sample is well-crystallized

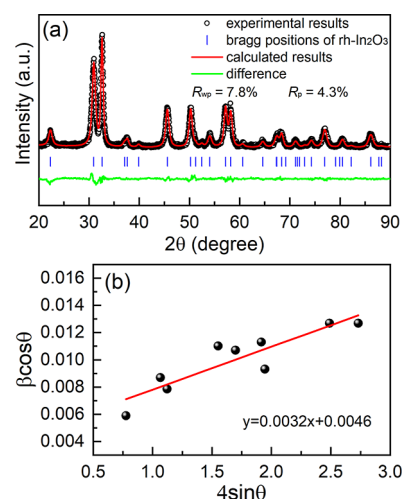


Figure 1. (a) Rietveld refinement of the XRD pattern and (b) Williamson–Hall plot of rh-In₂O₃ nanocrystals obtained at 400 °C.

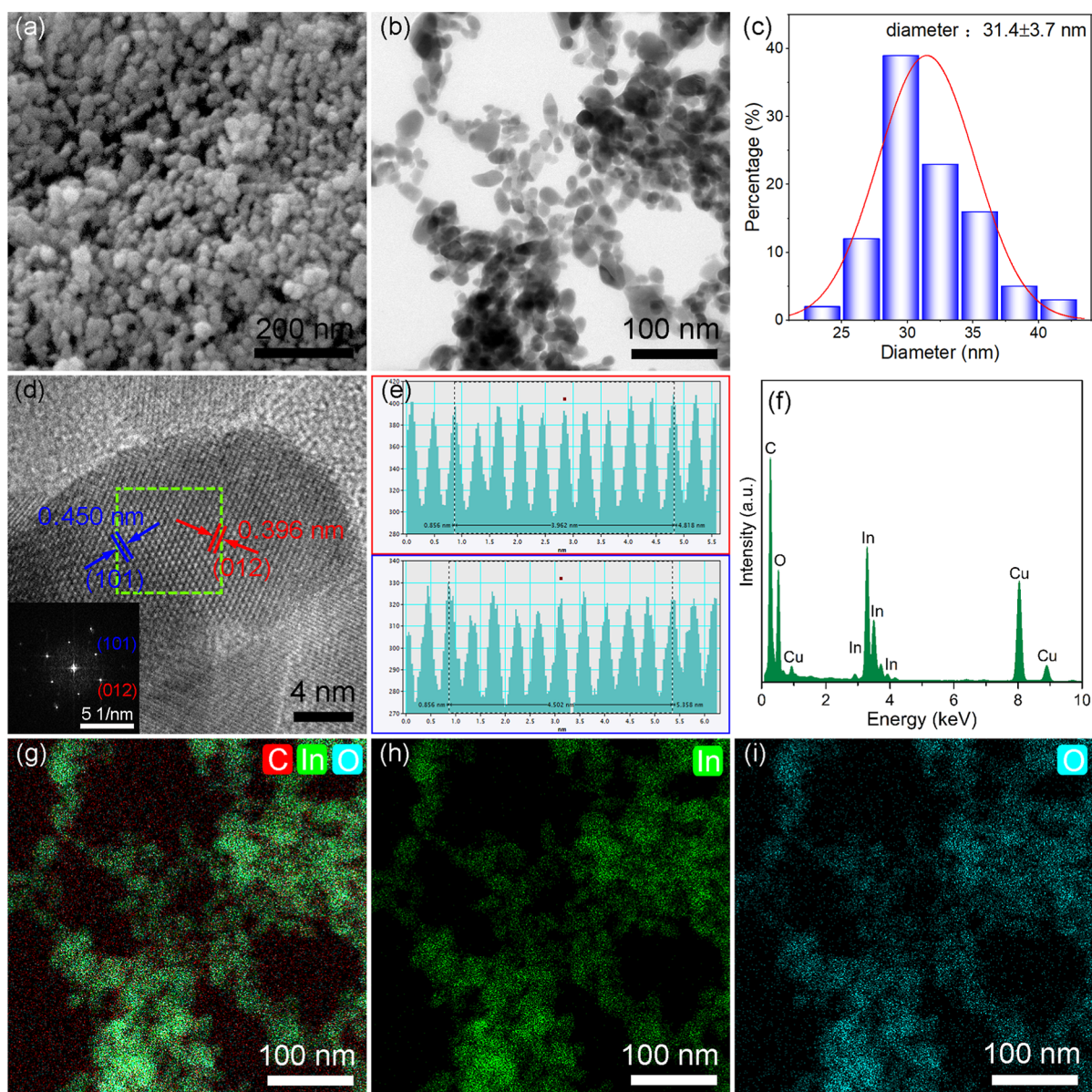


Figure 2. Typical (a) SEM and (b) TEM images of rh-In₂O₃ nanocrystals. (c) Distribution histogram of the particle size of the as-prepared rh-In₂O₃ nanocrystals. (d) HRTEM image and FFT pattern (inset) corresponding to the selected area (green dashed box in the HRTEM image) of a random nanoparticle and (e) screenshot showing the interplanar spacings of the (012) and (202) planes. (f) EDS spectrum of the prepared rh-In₂O₃ nanocrystals (the Cu element is detected from the supporting mesh). (g–i) EDS mapping images for the distribution of C, In, and O elements, respectively.

at 400 °C. The Rietveld refinement result reveals that the crystals are rh-In₂O₃ with the lattice parameters of $a = b = 5.4816(3)$ Å and $c = 14.507(2)$ Å. Their average crystallite size was estimated by the Williamson–Hall (W–H) equation³⁶

$$\beta_T \cos \theta = \varepsilon(4 \sin \theta) + \frac{K\lambda}{D} \quad (1)$$

where β_T is the broadening of the diffraction peak (the full width at half-maximum), ε is the strain, K ($=0.89$) is a constant, and λ , D , and θ are the wavelength of the X-ray, crystallites size, and peak position, respectively. The calculated result of the average crystallite size of the rh-In₂O₃ nanocrystals is about 30.2 nm (Figure 1b). This value is in good accord with the average particle size (31.4 nm shown in Figure 2c) directly observed from the SEM image (Figure 2a). Transmission electron microscopy (TEM) analysis (Figure 2b) further

confirms the transformation of InOOH nanowires into rh-In₂O₃ nanoparticles with an irregular morphology. According to the high-resolution (HR)TEM image of a random nanoparticle (Figure 2d), it is pretty obvious that these well-defined lattice planes reveal the single-crystalline nature of these nanoparticles. The HRTEM image also allows estimation of the crystalline interplanar spacing, which corresponds to the (012) and (101) lattice faces in the rh-In₂O₃ crystal structure, as confirmed by the calculated lattice distances (Figure 2e) and the corresponding fast Fourier transform (FFT) pattern (inset of Figure 2d). Moreover, the chemical composition of the annealed rh-In₂O₃ nanocrystals was seriously checked by energy-dispersive spectrometry (EDS) and XPS analyses. The typical EDS spectrum (Figure 2f) and EDS mapping images (Figure 2g–i) exhibit that In and O elements are uniformly distributed in these nanocrystals with the contents of about

38.6 and 61.4 at. %, respectively. Obviously, these values roughly match the nominal stoichiometry of In_2O_3 .

As shown in Figure 3, XPS analysis was further performed to determine the elemental composition and valence states of the

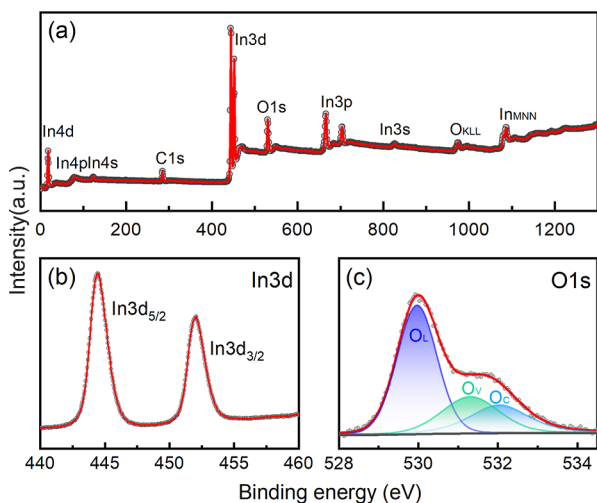


Figure 3. XPS spectra for (a) full scan survey, (b) In 3d, and (c) O 1s of rh- In_2O_3 nanocrystals.

rh- In_2O_3 nanocrystals. From Figure 3a, the signals of the In, O, and C elements can be easily found in the XPS full spectrum. The C 1s peak, located at 284.8 eV, is normally attributed to the adventitious contamination and used for calibrating the binding energies. The narrow-scan spectra of In 3d (Figure 3b) exhibit two distinct peaks corresponding to In 3d_{5/2} and In 3d_{3/2} at binding energies of 444.4 and 452.1 eV, respectively, confirming the presence of In in the In^{3+} state.^{26,37} Also, the high-resolution O 1s spectra with three deconvoluted peaks (marked as O_L, O_V, and O_C, respectively) are shown in Figure 3c. According to previous reports, O_L, O_V, and O_C peaks with binding energies of approximately 529.9, 531.3, and 532.1 eV are normally ascribed to the In–O bonding, oxygen vacancies, and surface-chemisorbed oxygen, respectively.^{38–40} It is reasonable that the hydroxyl species will release oxygen to form oxygen vacancies during the annealing processes.⁴¹ Furthermore, the presence of oxygen vacancies in the rh- In_2O_3 nanocrystals can also be visualized from the ESR spectrum. As shown in Figure S5, the rh- In_2O_3 nanocrystals

exhibit an obvious ESR signal at $g = 2.004$, which is usually ascribed to the typical signal of oxygen vacancies.^{18,42,43}

While annealed at 700 °C, it is quite apparent that the final product is entirely composed of c- In_2O_3 nanocrystals (Figure S6a). The morphology, size distribution, and elemental composition of these c- In_2O_3 nanoparticles were meticulously examined (Figures S6b,c and S7, respectively). It is apparent that the average diameter of these c- In_2O_3 nanoparticles (Figure S6b) is around 63.5 nm. XPS analysis indicates that these nanoparticles contain only In and O elements with an atomic ratio of about 1:1.43. This slight deviation from the nominal stoichiometry of In_2O_3 can be attributed to the presence of oxygen vacancies, as revealed in Figure S7c.

Finally, before evaluating the photocatalytic activity of these rh- In_2O_3 , c- In_2O_3 , and commercial P25– TiO_2 nanocrystals, their optical absorptions were essential to be studied. From Figure S8a, it is clear that P25– TiO_2 nanocrystals show strong photoabsorption in the UV region with an absorption edge of about 396 nm. In contrast, the rh- In_2O_3 and c- In_2O_3 nanocrystals display effective photoabsorption in both the UV and visible light regions up to 442 and 461 nm, respectively. It hints that the as-prepared rh- In_2O_3 and c- In_2O_3 nanocrystals can absorb more photons at the initial stage of the photodegradation process.³² Typically, their band gap values can be calculated by the following equation³²

$$\alpha h\nu^n = A(h\nu - E_g) \quad (2)$$

where α , $h\nu$, and E_g are the absorption coefficient, incident photon energy, and band gap energy, respectively. In this equation, A is a constant and $n = 1/2$ or 2 for an indirect or a direct semiconductor, respectively. As shown in Figure S8b, all of the rh- In_2O_3 , c- In_2O_3 , and P25– TiO_2 nanocrystals have a direct band gap with values of about 2.92, 2.74, and 3.20 eV, respectively. These calculated results tally with the band gaps reported in previous works and allow for the rh- In_2O_3 , c- In_2O_3 , and P25– TiO_2 nanocrystals to be better excited under the UV light region for enhancing their photocatalytic performance.^{44–49}

Photocatalytic Degradation of RIF. The photocatalytic activity of the as-prepared rh- In_2O_3 nanocrystals for the degradation of RIF under UV irradiation was evaluated by comparing them with c- In_2O_3 and commercial P25– TiO_2 nanocrystals. Initially, all suspensions that contain RIF (10 mg/L) and the photocatalysts (0.1 g/L) were kept in darkness

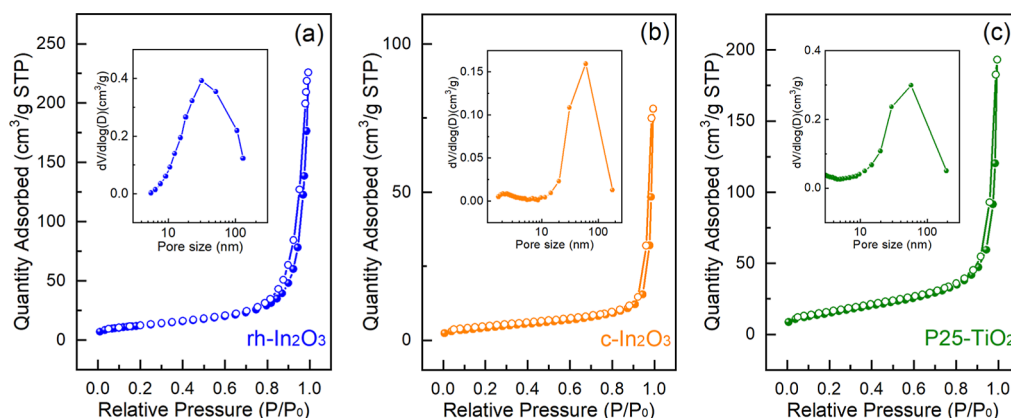


Figure 4. Nitrogen adsorption–desorption isotherms and the corresponding pore size distribution curves as the insets of (a) rh- In_2O_3 , (b) c- In_2O_3 , and (c) P25– TiO_2 nanocrystals.

for 1 h to establish the adsorption/desorption equilibrium. From Figure 4, it is clear that the rh-In₂O₃ and P25–TiO₂ nanocrystals possess larger specific surface areas (43.8 and 50.1 m² g⁻¹ shown in Figure 4a,c, respectively) than c-In₂O₃ nanocrystals (14.3 m² g⁻¹ shown in Figure 4b). However, all the three photocatalysts exhibited poor adsorption capacities for RIF, showing no significant difference (Figure S9). By the way, consider that the average particle sizes of rh-In₂O₃, c-In₂O₃, and P25–TiO₂ nanocrystals are about 30, 63, and 25 nm, respectively; thus, the pores with sizes around 20–100 nm observed in the three samples should be attributed to the interstices among different nanocrystals. During the irradiation process, without photocatalysts, RIF degradation could be almost ignored (Figure 5b). For rh-In₂O₃ nanocrystals as

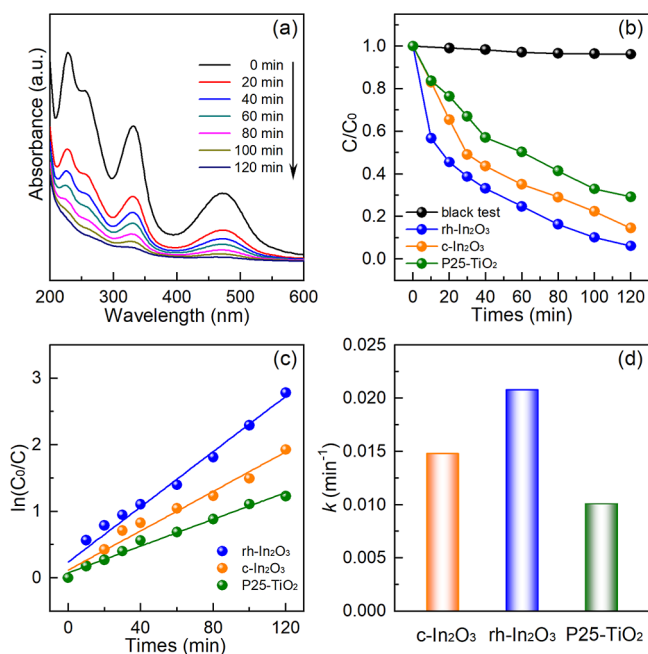


Figure 5. (a) Variation of UV–vis absorption spectra of RIF over rh-In₂O₃ nanocrystals (0.1 g/L) under UV irradiation. (b) Time-dependent normalized concentrations of RIF solutions in the presence of different catalysts. (c) Plots of $\ln(C_0/C)$ against the irradiation time, fitted by using the pseudo-first-order model with the photodegradation rates shown in (d).

photocatalysts, the RIF concentration decreased dramatically in the first 20 min. Then, with the extension of irradiation time, the concentration diminished continuously, accompanied by the destruction of the molecular structure of RIF, which can be reflected by the temporal absorption spectral changes of RIF solutions shown in Figure 5a. After irradiation for 120 min, the highest RIF degradation rate reached about 94%, while the degradation rates of c-In₂O₃ and commercial P25–TiO₂ nanocrystals were only 85 and 71%, respectively, under the same conditions.

Furthermore, in order to compare the photodegradation efficiencies of RIF over different catalysts, the kinetic curves were simulated following the pseudo-first-order kinetic equation⁵⁰

$$\ln(C_0/C) = kt \quad (3)$$

where k is the pseudo-first-order rate constant and C_0 and C are the concentrations of solution at equilibrium and different

irradiation times, respectively. As shown in Figure 5c,d, the linear fitting results demonstrate that these photodegradation processes follow pseudo-first-order behavior, and the corresponding reaction rate constants further confirm that the rh-In₂O₃ sample (0.0208 min⁻¹) exhibits better photocatalytic performance than the c-In₂O₃ (0.0148 min⁻¹) and commercial P25–TiO₂ (0.0101 min⁻¹) nanocrystals.

The apparent quantum efficiency (Φ_{AQE}), which is a crucial parameter for evaluating the performance of a photocatalyst in a homogeneous system, is commonly defined as⁵¹

$$\Phi_{AQE} = \frac{\text{rate of reaction}}{\text{flux of incident photons}} = \frac{dx/dt}{q_\lambda [1 - 10^{-A}]} \quad (4)$$

where dx/dt is the change rate of the number of pollutant molecules, q_λ is the number of photons incident per time interval, and A is the absorbance. In our study, the apparent quantum efficiencies of rh-In₂O₃, c-In₂O₃, and P25–TiO₂ nanocrystals on the photocatalytic degradation of RIF could be determined as

$$\Phi_{AQE} = \frac{kVC_0e^{-kt}}{[1 - 10^{-\epsilon C \Delta L}] I_{inc} S / U_{\lambda=365}} \quad (5)$$

where k is the pseudo-first-order rate constant, C_0 is the concentration of solution at equilibrium, V is the total liquid volume in the reactor, ϵ is the molar extinction coefficient, ΔL is the length of the light path, I_{inc} is the incident light intensity, S is the illuminated area, and $U_{\lambda=365}$ is the energy of 1 mol of photons. According to the parameters shown in Tables S2 and S3 and Figure S10, the results of the apparent quantum efficiencies of rh-In₂O₃, c-In₂O₃, and P25–TiO₂ nanocrystals on the photocatalytic degradation of RIF were obtained (Figure 6). It is obvious that rh-In₂O₃ exhibits a higher

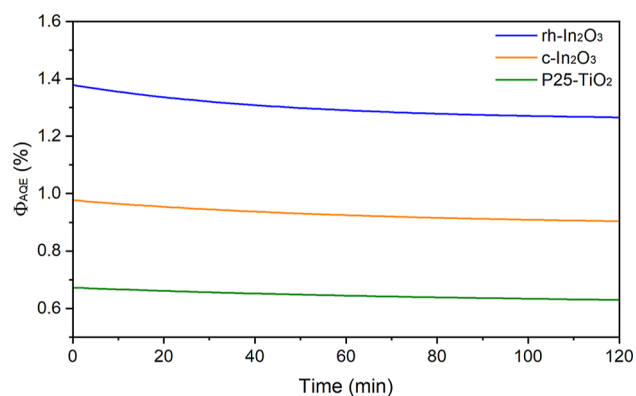


Figure 6. Plots of the apparent quantum efficiencies of rh-In₂O₃, c-In₂O₃, and P25–TiO₂ nanocrystals against irradiation time.

photonic efficiency and is therefore a more efficient photocatalyst. It is generally accepted that the specific surface area, which is a key factor, can affect the photocatalytic activity of materials. Materials with larger specific surface areas typically demonstrate superior photocatalytic activity due to a greater number of reactive adsorption/desorption sites available during the photocatalytic reactions.³³ Interestingly, in our case, P25–TiO₂ possesses the largest specific surface area but exhibits the lowest efficiency in the photodegradation of RIF. Therefore, this discrepancy cannot be simply explained by the effect of the specific surface area.

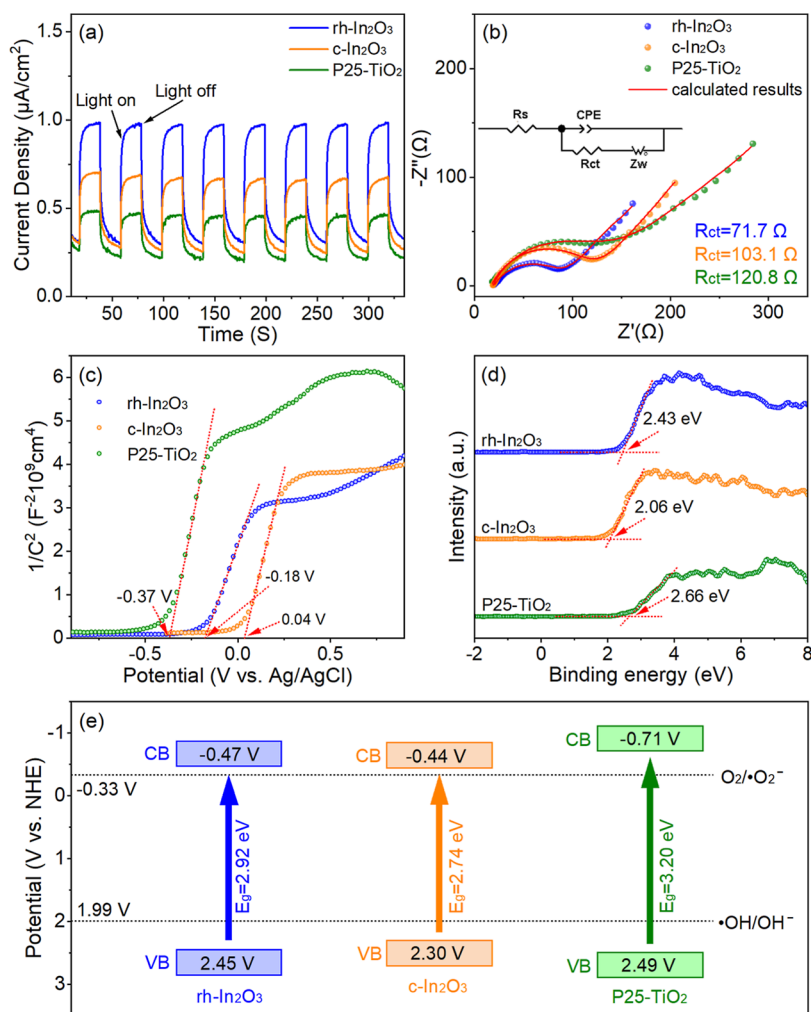


Figure 7. (a) Transient photocurrent curves. (b) Circuit-fitted Nyquist plots. The inset is the electrical equivalent circuit, which consists of electrolyte resistance (R_s), charge-transfer resistance (R_{ct}), double-layer capacitance (CPE), and Warburg impedance (Z_w). (c) Mott–Schottky plots. (d) Valence band XPS spectra. (e) Schematic band structures of rh- In_2O_3 , c- In_2O_3 , and P25- TiO_2 nanocrystals obtained according to (c,d).

Considering the generation and transfer of photogenerated electrons and holes can also severely impact the photocatalytic performance of rh- In_2O_3 , c- In_2O_3 , and P25- TiO_2 nanocrystals; thus, their photoelectrochemical properties were carefully checked.^{10,41,52–54} Obviously, from the transient photocurrent spectra demonstrated in Figure 7a, both rh- In_2O_3 and c- In_2O_3 display significantly enhanced photocurrent compared with P25- TiO_2 nanocrystals. rh- In_2O_3 presents the highest transient photocurrent response, revealing a more efficient separation and transfer process of photogenic electron–hole pairs in the rh- In_2O_3 nanocrystals.¹⁰ This observation is further supported by the electrochemical impedance measurement results illustrated in Figure 7b. It is obvious that each Nyquist plot consists of one depressed semicircle in the high-frequency region and a sloping straight line in the low-frequency region. It is generally accepted that the high-frequency semicircle is related to the charge-transfer resistance at the interface (R_{ct}), while the sloping straight line can be ascribed to the diffusion-controlled process (Warburg impedance).⁵⁵ To better understand the Nyquist plots, an equivalent circuit (inset of Figure 7b) was proposed, and the impedance parameters were simulated using Zview software. The calculated value of R_{ct} of the rh- In_2O_3 nanocrystals (71.7 Ω) is significantly smaller than that of c- In_2O_3 (103.1 Ω) and P25- TiO_2 (120.8 Ω)

nanocrystals, demonstrating a higher photogenerated electron–hole separation and transfer efficiency in these rh- In_2O_3 nanocrystals.⁵⁶ Based on the above-mentioned discussion, we can recognize that rh- In_2O_3 has only a slightly smaller specific surface area but much better performance on separation and transfer of photogenerated electron–hole pairs compared to P25- TiO_2 . Therefore, it is hardly surprising that it has the best efficiency in the photodegradation of RIF. In addition, after a four-circle photodegradation process under the same conditions, it is noticeable that its photocatalytic activity and structure exhibit considerable stability (Figures S11–S14).

Photocatalytic Degradation Mechanism. In order to understand the photocatalytic degradation process of RIF intuitively, the possible degradation pathways are proposed by identifying the yielded intermediates (Table S4) via UPLC-HRMS (Figures S15 and S16). As depicted in Figure 8, two distinct transformation pathways for RIF photodegradation have been identified. For pathway I, some RIF molecules could be transformed to RIF 1 and RIF 2 successively through the opening of the piperazine ring, hydroxylation, dehydration, and demethylation reactions. Under further oxidation, the intermediates RIF 3 and RIF 4 were obtained. Then, they could be decomposed to the detected compounds RIF 5 and RIF 6, respectively, by the opening of nitrogen-bearing heterocyclic

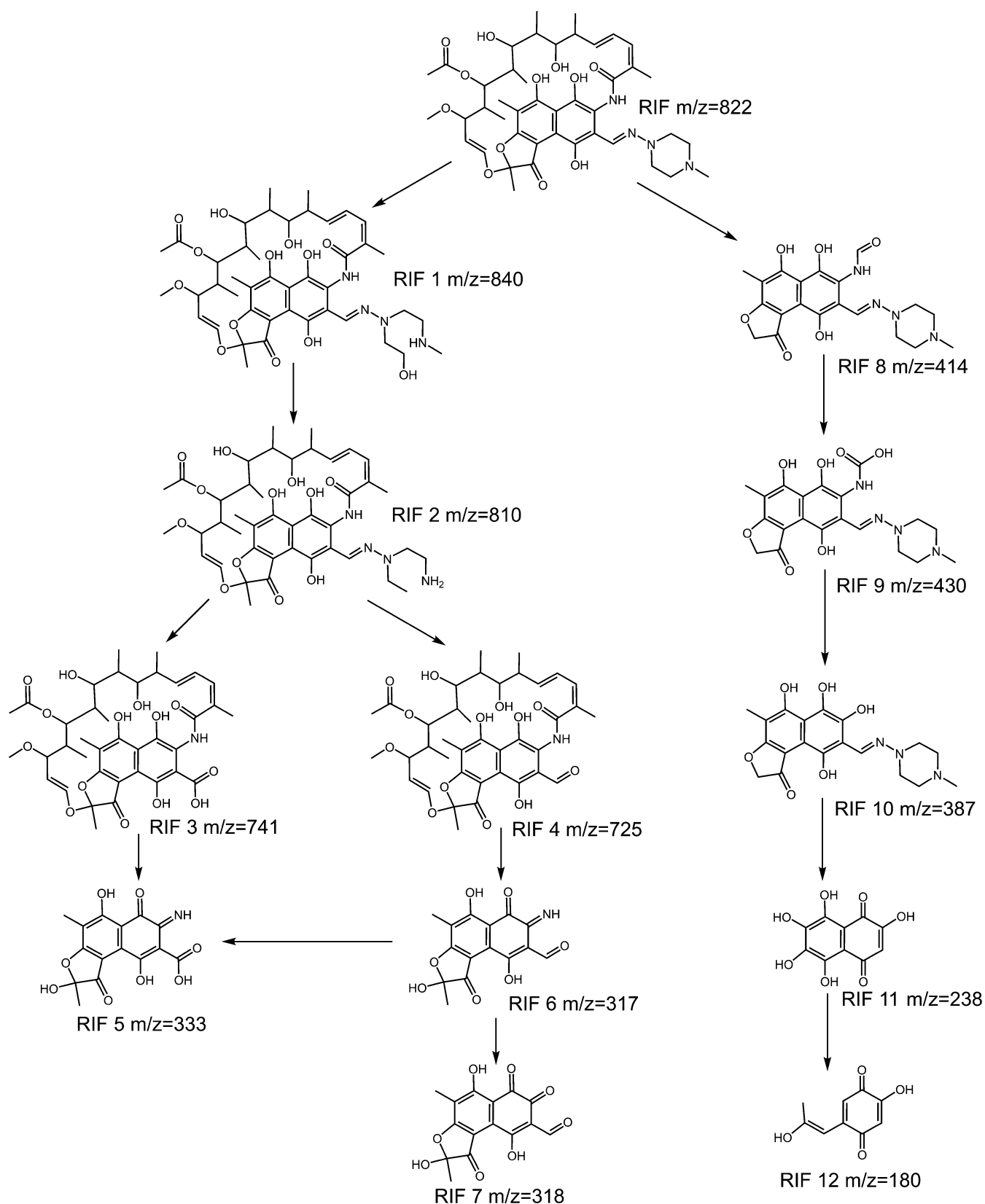


Figure 8. Probable photocatalytic degradation pathway of RIF over $\text{rh-In}_2\text{O}_3$ nanocrystals.

and chain scission. Next, RIF 6 could be directly oxidized to RIF 5 and RIF 7. As for pathway II, RIF was first degraded to RIF 8 via the opening of nitrogen-bearing heterocyclic and chain scission. On successive oxidation, decarboxylation, and

hydrolysis, RIF 9 and RIF 10 were produced. Subsequently, RIF 10 could be decomposed to RIF 11 by a series of reactions including cleavage of the piperazine side chain, decarboxylation, oxidation, hydroxylation, and cleavage of the oxygen

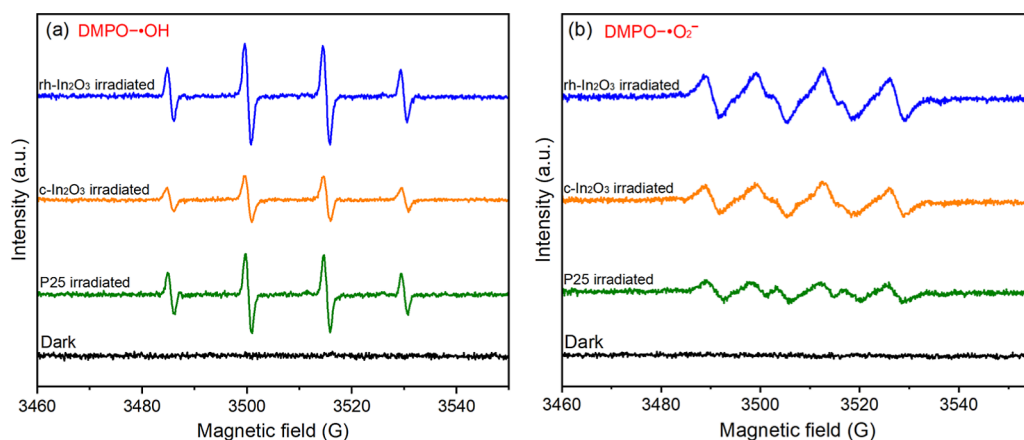


Figure 9. ESR spectra of $\cdot\text{OH}$ and $\cdot\text{O}_2^-$ radicals trapped by DMPO.

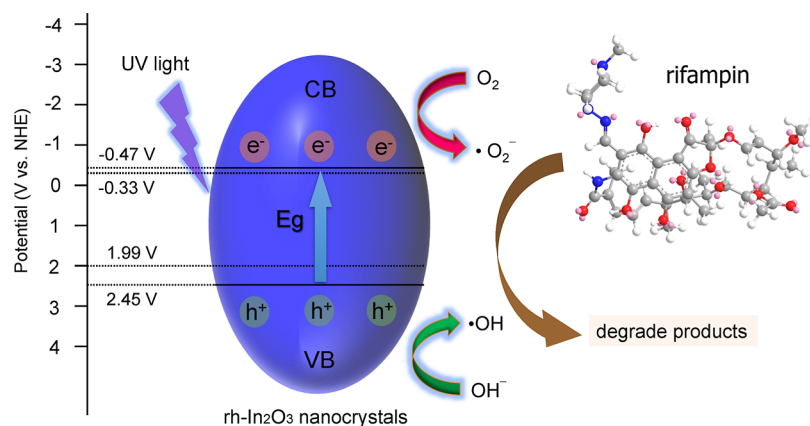


Figure 10. Possible mechanism for the photodegradation of RIF over rh-In₂O₃ nanocrystals.

heterocyclic ring attacked by hydroxyl radicals. Then, further oxidation caused the opening of the aromatic ring, and RIF 12 was obtained. Ultimately, these small molecules might be further mineralized to CO₂ and H₂O.¹²

As is well known, reactive species, such as electrons (e^-), holes (h^+), superoxide radicals ($\cdot\text{O}_2^-$), and hydroxyl radicals ($\cdot\text{OH}$), play vital roles during the photodegradation processes. In addition, their generation is closely relevant to the band structures of the photocatalyst.^{52,57} Hence, in order to seek the mechanism of the photocatalytic degradation of RIF over rh-In₂O₃ nanocrystals, their valence band (E_{VB}) and conduction band (E_{CB}) energies were further determined by the VB-XPS spectrum and the M-S plot. As shown in Figure 7c, a positive slope line implies that the rh-In₂O₃ sample is an n-type semiconductor. Meanwhile, its flat band potential (V_{fb}) can be estimated to be about -0.18 eV vs Ag/AgCl or 0.02 eV vs NHE. Consequently, it can be inferred that the Fermi level (E_{f}) of rh-In₂O₃ is 0.02 V (vs NHE) since V_{fb} is nearly equal to E_{f} for n-type semiconductors.⁴ Simultaneously, the VB-XPS spectrum (Figure 7d) displays that the energy difference between E_{f} and E_{VB} is approximately 2.43 eV.^{17,18} Therefore, as shown in Figure 7e, the E_{VB} value of rh-In₂O₃ is calculated to be 2.45 V vs NHE, and the E_{CB} value can be confirmed to be -0.47 V vs NHE according to a simple formula ($E_{\text{CB}} = E_{\text{VB}} - E_{\text{g}}$). The calculated results show that the E_{CB} value is more negative than $E^\circ(\text{O}_2/\cdot\text{O}_2^-)$ (-0.33 V vs NHE) and E_{VB} is more positive than $E^\circ(\cdot\text{OH}/\text{OH}^-)$ (1.99 V vs NHE). Theoretically, the photogenerated electrons can react with

O₂ to form $\cdot\text{O}_2^-$, while OH⁻ can be oxidized by holes to produce $\cdot\text{OH}$.^{10,50} Furthermore, ESR analysis with 5,5-dimethyl-1-pyrroline *N*-oxide (DMPO) serving as the trapping agent was employed to identify whether $\cdot\text{O}_2^-$ and $\cdot\text{OH}$ radicals were generated during the photodegradation process. As shown in Figure 9a,b, no signal of DMPO- $\cdot\text{O}_2^-$ or DMPO- $\cdot\text{OH}$ was detected under the dark condition. However, after 5 min of UV irradiation, four strong characteristic peaks with an intensity ratio of 1:2:2:1 could be detected and ascribed to the signal of DMPO- $\cdot\text{OH}$, while a weaker signal of DMPO- $\cdot\text{O}_2^-$ could also be observed.^{10,53} Therefore, these experimental results coincide with the theoretical analysis that both $\cdot\text{O}_2^-$ and $\cdot\text{OH}$ radicals could be produced during the photodegradation process.

For c-In₂O₃ and P25-TiO₂ nanocrystals, the theoretical calculation (Figure 7e) and ESR analysis (Figure 9) also show that both the $\cdot\text{O}_2^-$ and $\cdot\text{OH}$ radicals were generated during each photodegradation process. Notably, the intensities of DMPO- $\cdot\text{OH}$ and DMPO- $\cdot\text{O}_2^-$ signals of irradiated rh-In₂O₃ nanocrystals are stronger than those of c-In₂O₃ and P25-TiO₂ nanocrystals in the same conditions. In other words, rh-In₂O₃ nanocrystals as the photocatalyst yield higher amounts of $\cdot\text{O}_2^-$ and $\cdot\text{OH}$ radicals.¹⁰ This is likely the key factor contributing to the superior efficiency of rh-In₂O₃ nanocrystals in the photodegradation of RIF, compared to c-In₂O₃ and P25-TiO₂ nanocrystals.

To sum up, a reasonable mechanism for the photocatalytic degradation of rifampin is suggested (Figure 10). First, under

the irradiation of UV light, the photogenerated electron–hole pairs were generated and then transferred to the surface of the rh-In₂O₃ nanocrystals (when $h\nu = E_g$). Subsequently, these photogenerated electrons could reduce O₂ to produce $\cdot\text{O}_2^-$. In contrast, the photogenerated holes could oxidize OH⁻/H₂O to form $\cdot\text{OH}$. Ultimately, both the $\cdot\text{O}_2^-$ and $\cdot\text{OH}$ radicals would attack and break rifampin into small molecules.

CONCLUSIONS

In summary, rh-In₂O₃ nanoparticles with an average size of around 30 nm were successfully prepared via a facile hydrothermal method combined with a simple calcining process. Compared with c-In₂O₃ and P25–TiO₂ nanoparticles, rh-In₂O₃ nanoparticles demonstrated superior efficiency in the degradation of rifampin under UV light irradiation. The enhanced photoactivity is likely due to the more efficient separation and transfer of photogenic electron–hole pairs. Also, the feasible degradation pathways and mechanism of RIF were proposed by UHPLC–HRMS and ESR analyses. Moreover, this work presents a promising and low/no-toxicity photocatalyst for the efficient removal of antibiotics.

ASSOCIATED CONTENT

Supporting Information

The Supporting Information is available free of charge at <https://pubs.acs.org/doi/10.1021/acsomega.3c02652>.

Structural parameters of c-In₂O₃ and rh-In₂O₃; XRD pattern and TEM image of ultrathin InOOH nanowires; schematic illustration, dimensions, and main characteristics of the photocatalytic reactor; XRD patterns, TEM images, and SEM images of the samples prepared by annealing InOOH nanowires at different temperatures; ESR spectra of the rh-In₂O₃ nanocrystals; XRD pattern, SEM image, distribution histogram of the particle size, and XPS spectra of the c-In₂O₃ nanocrystals; typical absorption spectra of the rh-In₂O₃, rh-In₂O₃, and P25–TiO₂ nanocrystals; adsorption kinetics of rifampin on rh-In₂O₃, c-In₂O₃, and P25–TiO₂ nanocrystals; cycling runs in photocatalytic degradation of rifampin by rh-In₂O₃ nanocrystals; XRD patterns, nitrogen adsorption–desorption isotherms, and XPS spectra of rh-In₂O₃ before and after the photocatalytic reaction; and identified intermediates and their MS/MS spectra from photocatalytic degradation RIF over rh-In₂O₃ (PDF)

AUTHOR INFORMATION

Corresponding Author

Xianbo Xiao – School of Computer Science, Jiangxi University of Chinese Medicine, Nanchang 330004, China;
Email: 20101034@jxutcm.edu.cn

Authors

Shunxi Tang – School of Computer Science, Jiangxi University of Chinese Medicine, Nanchang 330004, China;
orcid.org/0000-0002-8417-0263

Xinyou Zhang – School of Computer Science, Jiangxi University of Chinese Medicine, Nanchang 330004, China

Shufeng Li – School of Pharmacy, Jiangxi University of Chinese Medicine, Nanchang 330004, China

Chupei Zheng – School of Pharmacy, Jiangxi University of Chinese Medicine, Nanchang 330004, China

Huili Li – School of Computer Science, Jiangxi University of Chinese Medicine, Nanchang 330004, China

Complete contact information is available at:
<https://pubs.acs.org/10.1021/acsomega.3c02652>

Notes

The authors declare no competing financial interest.

ACKNOWLEDGMENTS

This work was supported in part by the National Natural Science Foundation of China (grant nos. 12164021 and 11664019), the Natural Science Foundation of Jiangxi Province (grant no. 20212ACB201005), and the Jiangxi University of Traditional Chinese Medicine 1050 youth talent project (grant no. 5142001010).

REFERENCES

- (1) Raeisi-Kheirabadi, N.; Nezamzadeh-Ejehieh, A. A Z-Scheme g-C₃N₄/Ag₃PO₄ Nanocomposite: Its Photocatalytic Activity and Capability for Water Splitting. *Int. J. Hydrogen Energy* **2020**, *45* (58), 33381–33395.
- (2) Xu, Q.; Owens, G.; Chen, Z. Adsorption and Catalytic Reduction of Rifampicin in Wastewaters Using Hybrid RGO@Fe/Pd Nanoparticles. *J. Cleaner Prod.* **2020**, *264*, 121617.
- (3) Thuy, H. T. T.; Loan, T. T. C. Degradation of Selected Pharmaceuticals in Coastal Wetland Water and Sediments. *Water, Air, Soil Pollut.* **2014**, *225* (5), 1940.
- (4) Li, C.; Sun, T.; Zhang, D.; Zhang, X.; Qian, Y.; Zhang, Y.; Lin, X.; Liu, J.; Zhu, L.; Wang, X.; Shi, Z.; Lin, Q. Fabrication of Ternary Ag/La-Black TiO_{2-x} Photocatalyst with Enhanced Visible-Light Photocatalytic Activity for Tetracycline Degradation. *J. Alloys Compd.* **2022**, *891*, 161960.
- (5) Sadeghi Rad, T.; Khataee, A.; Arefi-Oskoui, S.; Sadeghi Rad, S.; Orooji, Y.; Gengec, E.; Kobya, M. Graphene-Based ZnCr Layered Double Hydroxide Nanocomposites as Bactericidal Agents with High Sonophotocatalytic Performances for Degradation of Rifampicin. *Chemosphere* **2022**, *286*, 131740.
- (6) Cai, W.; Weng, X.; Chen, Z. Highly Efficient Removal of Antibiotic Rifampicin from Aqueous Solution Using Green Synthesis of Recyclable Nano-Fe₃O₄. *Environ. Pollut.* **2019**, *247*, 839–846.
- (7) Zou, R.; Xu, T.; Lei, X.; Wu, Q.; Xue, S. Novel and Efficient Red Phosphorus/Hollow Hydroxyapatite Microsphere Photocatalyst for Fast Removal of Antibiotic Pollutants. *J. Phys. Chem. Solids* **2020**, *139*, 109353.
- (8) Kais, H.; Mezenner, N. Y.; Trari, M.; Madjene, F. Photocatalytic Degradation of Rifampicin: Influencing Parameters and Mechanism. *Russ. J. Phys. Chem.* **2019**, *93* (13), 2834–2841.
- (9) Khataee, A.; Gholami, P.; Kayan, B.; Kalderis, D.; Dinpazhoh, L.; Akay, S. Synthesis of ZrO₂ Nanoparticles on Pumice and Tuff for Sonocatalytic Degradation of Rifampin. *Ultrason. Sonochem.* **2018**, *48*, 349–361.
- (10) Zhuang, Y.; Luan, J. Improved Photocatalytic Property of Peony-like InOOH for Degrading Norfloxacin. *Chem. Eng. J.* **2020**, *382*, 122770.
- (11) Wang, X.; Li, Z.; Zhang, Y.; Li, Q.; Du, H.; Liu, F.; Zhang, X.; Mu, H.; Duan, J. Enhanced Photocatalytic Antibacterial and Degradation Performance by P-n-p Type CoFe₂O₄/CoFe₂S₄/MgBi₂O₆ Photocatalyst under Visible Light Irradiation. *Chem. Eng. J.* **2022**, *429*, 132270.
- (12) Gao, B.; Dong, S.; Liu, J.; Liu, L.; Feng, Q.; Tan, N.; Liu, T.; Bo, L.; Wang, L. Identification of Intermediates and Transformation Pathways Derived from Photocatalytic Degradation of Five Antibiotics on ZnIn₂S₄. *Chem. Eng. J.* **2016**, *304*, 826–840.
- (13) Xekoukoulotakis, N. P.; Xinidis, N.; Chroni, M.; Mantzavinos, D.; Venieri, D.; Hapeshi, E.; Fatta-Kassinos, D. UV-A/TiO₂ Photocatalytic Decomposition of Erythromycin in Water: Factors

- Affecting Mineralization and Antibiotic Activity. *Catal. Today* **2010**, *151* (1–2), 29–33.
- (14) Wang, J.; Tafen, D. N.; Lewis, J. P.; Hong, Z.; Manivannan, A.; Zhi, M.; Li, M.; Wu, N. Origin of Photocatalytic Activity of Nitrogen-Doped TiO₂ Nanobelts. *J. Am. Chem. Soc.* **2009**, *131* (34), 12290–12297.
- (15) Li, Z.; Zhang, P.; Shao, T.; Wang, J.; Jin, L.; Li, X. Different Nanostructured In₂O₃ for Photocatalytic Decomposition of Perfluorooctanoic Acid (PFOA). *J. Hazard. Mater.* **2013**, *260*, 40–46.
- (16) Zhang, X.; Qin, J.; Xue, Y.; Yu, P.; Zhang, B.; Wang, L.; Liu, R. Effect of Aspect Ratio and Surface Defects on the Photocatalytic Activity of ZnO Nanorods. *Sci. Rep.* **2014**, *4* (1), 4596.
- (17) Han, L.; Jing, F.; Zhang, J.; Luo, X.-Z.; Zhong, Y.-L.; Wang, K.; Zang, S.-H.; Teng, D.-H.; Liu, Y.; Chen, J.; Yang, C.; Zhou, Y.-T. Environment Friendly and Remarkably Efficient Photocatalytic Hydrogen Evolution Based on Metal Organic Framework Derived Hexagonal/Cubic In₂O₃ Phase-Junction. *Appl. Catal., B* **2021**, *282*, 119602.
- (18) Lei, F.; Sun, Y.; Liu, K.; Gao, S.; Liang, L.; Pan, B.; Xie, Y. Oxygen Vacancies Confined in Ultrathin Indium Oxide Porous Sheets for Promoted Visible-Light Water Splitting. *J. Am. Chem. Soc.* **2014**, *136* (19), 6826–6829.
- (19) Korotcenkov, G.; Brinzari, V.; Nehasil, V. XPS Study of Rh/In₂O₃ System. *Surf. Interfaces* **2021**, *22*, 100794.
- (20) Tang, S.; Li, Y.; Zhang, J.; Zhu, H.; Dong, Y.; Zhu, P.; Cui, Q. Effects of Microstructures on the Compression Behavior and Phase Transition Routine of In₂O₃ Nanocubes under High Pressures. *RSC Adv.* **2015**, *5* (103), 85105–85110.
- (21) García-Domene, B.; Sans, J. A.; Manjón, F. J.; Ovsyannikov, S. V.; Dubrovinsky, L. S.; Martínez-García, D.; Gomis, O.; Errandonea, D.; Moutaabbid, H.; Le Godec, Y.; Ortiz, H. M.; Muñoz, A.; Rodríguez-Hernández, P.; Popescu, C. Synthesis and High-Pressure Study of Corundum-Type In₂O₃. *J. Phys. Chem. C* **2015**, *119* (52), 29076–29087.
- (22) Su, M.; Zou, X.; Gong, Y.; Wang, J.; Liu, Y.; Ho, J. C.; Liu, X.; Liao, L. Sub-KT/q Switching in In₂O₃ Nanowire Negative Capacitance Field-Effect Transistors. *Nanoscale* **2018**, *10* (40), 19131–19139.
- (23) Wang, B.; Zheng, Z.; Wu, H.; Zhu, L. Field Emission Properties and Growth Mechanism of In₂O₃ Nanostructures. *Nanoscale Res. Lett.* **2014**, *9* (1), 111.
- (24) Senapati, S.; Nanda, K. K. Wide-Range Thermometry at Micro/Nano Length Scales with In₂O₃ Octahedrons as Optical Probes. *ACS Appl. Mater. Interfaces* **2015**, *7* (42), 23481–23488.
- (25) Jiang, H.; Zhao, L.; Gai, L.; Ma, L.; Ma, Y.; Li, M. Hierarchical Rh-In₂O₃ Crystals Derived from InOOH Counterparts and Their Sensitivity to Ammonia Gas. *CrystEngComm* **2013**, *15* (35), 7003.
- (26) Geng, Q.; Karkyngul, B.; Sun, C.; Liang, X.; Yang, C.; Su, X. In₂O₃ Nanocubes Derived from Monodisperse InOOH Nanocubes: Synthesis and Applications in Gas Sensors. *J. Mater. Sci.* **2017**, *52* (9), 5097–5105.
- (27) Li, P.; Fan, H.; Cai, Y.; Xu, M.; Long, C.; Li, M.; Lei, S.; Zou, X. Phase Transformation (Cubic to Rhombohedral): The Effect on the NO₂ Sensing Performance of Zn-Doped Flower-like In₂O₃ Structures. *RSC Adv.* **2014**, *4* (29), 15161.
- (28) Chen, F.; Yang, M.; Wang, X.; Song, Y.; Guo, L.; Xie, N.; Kou, X.; Xu, X.; Sun, Y.; Lu, G. Template-Free Synthesis of Cubic-Rhombohedral-In₂O₃ Flower for Ppb Level Acetone Detection. *Sens. Actuators, B* **2019**, *290*, 459–466.
- (29) Sui, N.; Cao, S.; Zhang, P.; Zhou, T.; Zhang, T. The Effect of Different Crystalline Phases of In₂O₃ on the Ozone Sensing Performance. *J. Hazard. Mater.* **2021**, *418*, 126290.
- (30) Yin, J.; Cao, H. Synthesis and Photocatalytic Activity of Single-Crystalline Hollow Rh-In₂O₃ Nanocrystals. *Inorg. Chem.* **2012**, *51* (12), 6529–6536.
- (31) Wu, M.; Wang, C.; Zhao, Y.; Xiao, L.; Zhang, C.; Yu, X.; Luo, B.; Hu, B.; Fan, W.; Shi, W. Hydrothermal Synthesis of Porous Rh-In₂O₃ Nanostructures with Visible-Light-Driven Photocatalytic Degradation of Tetracycline. *CrystEngComm* **2015**, *17* (11), 2336–2345.
- (32) Zhou, B.; Li, Y.; Bai, J.; Li, X.; Li, F.; Liu, L. Controlled Synthesis of Rh-In₂O₃ Nanostructures with Different Morphologies for Efficient Photocatalytic Degradation of Oxytetracycline. *Appl. Surf. Sci.* **2019**, *464*, 115–124.
- (33) Tang, S.; Zhang, C.; Chen, T.; Du, Y.; Xiao, X. Enhanced Photocatalytic Activity of Ultrathin InOOH Nanowires. *Appl. Surf. Sci.* **2021**, *562*, 150225.
- (34) Parasuraman, R.; Wu, Y.; Ordonez-Miranda, J.; Volz, S.; Umarji, A. M. Particle Size Effect on the Thermal Conductivity Reduction of Silicon Based Thermoelectric Composites. *Sustain. Energy Fuels* **2018**, *2* (8), 1764–1771.
- (35) Tominaka, S.; Hamoudi, H.; Suga, T.; Bennett, T. D.; Cairns, A. B.; Cheetham, A. K. Topochemical Conversion of a Dense Metal-Organic Framework from a Crystalline Insulator to an Amorphous Semiconductor. *Chem. Sci.* **2015**, *6* (2), 1465–1473.
- (36) Brandstetter, S.; Derlet, P. M.; Van Petegem, S.; Van Swygenhoven, H. Williamson-Hall Anisotropy in Nanocrystalline Metals: X-Ray Diffraction Experiments and Atomistic Simulations. *Acta Mater.* **2008**, *56* (2), 165–176.
- (37) Wang, J.; Sun, K.; Jia, X.; Liu, C. CO₂ Hydrogenation to Methanol over Rh/In₂O₃ Catalyst. *Catal. Today* **2021**, *365*, 341–347.
- (38) Wang, L.; Dong, Y.; Yan, T.; Hu, Z.; Ali, F. M.; Meira, D. M.; Duchesne, P. N.; Loh, J. Y. Y.; Qiu, C.; Storey, E. E.; Xu, Y.; Sun, W.; Ghousoub, M.; Kherani, N. P.; Helmy, A. S.; Ozin, G. A. Black Indium Oxide a Photothermal CO₂ Hydrogenation Catalyst. *Nat. Commun.* **2020**, *11* (1), 2432.
- (39) Yan, T.; Li, N.; Wang, L.; Ran, W.; Duchesne, P. N.; Wan, L.; Nguyen, N. T.; Wang, L.; Xia, M.; Ozin, G. A. Bismuth Atom Tailoring of Indium Oxide Surface Frustrated Lewis Pairs Boosts Heterogeneous CO₂ Photocatalytic Hydrogenation. *Nat. Commun.* **2020**, *11* (1), 6095.
- (40) Gan, J.; Lu, X.; Wu, J.; Xie, S.; Zhai, T.; Yu, M.; Zhang, Z.; Mao, Y.; Wang, S. C. I.; Shen, Y.; Tong, Y. Oxygen Vacancies Promoting Photoelectrochemical Performance of In₂O₃ Nanocubes. *Sci. Rep.* **2013**, *3* (1), 1021.
- (41) Xu, H.; Wang, Y.; Dong, X.; Zheng, N.; Ma, H.; Zhang, X. Fabrication of In₂O₃/In₂S₃ Microsphere Heterostructures for Efficient and Stable Photocatalytic Nitrogen Fixation. *Appl. Catal., B* **2019**, *257*, 117932.
- (42) Arooj, S.; Xu, T.; Hou, X.; Wang, Y.; Tong, J.; Chu, R.; Liu, B. Green Emission of Indium Oxide via Hydrogen Treatment. *RSC Adv.* **2018**, *8* (21), 11828–11833.
- (43) Qi, Y.; Jiang, J.; Liang, X.; Ouyang, S.; Mi, W.; Ning, S.; Zhao, L.; Ye, J. Fabrication of Black In₂O₃ with Dense Oxygen Vacancy through Dual Functional Carbon Doping for Enhancing Photothermal CO₂ Hydrogenation. *Adv. Funct. Mater.* **2021**, *31* (22), 2100908.
- (44) de Boer, T.; Bekheet, M. F.; Gurlo, A.; Riedel, R.; Moewes, A. Band Gap and Electronic Structure of Cubic, Rhombohedral, and Orthorhombic In₂O₃ Polymorphs: Experiment and Theory. *Phys. Rev. B* **2016**, *93* (15), 155205.
- (45) King, P. D. C.; Veal, T. D.; Fuchs, F.; Wang, Ch. Y.; Payne, D. J.; Bourlange, A.; Zhang, H.; Bell, G. R.; Cimalla, V.; Ambacher, O.; Egdel, R. G.; Bechstedt, F.; McConville, C. F. Band Gap, Electronic Structure, and Surface Electron Accumulation of Cubic and Rhombohedral In₂O₃. *Phys. Rev. B: Condens. Matter Mater. Phys.* **2009**, *79* (20), 205211.
- (46) Singhal, A.; Jain, D.; Pai, M. R.; Agouram, S.; Errandonea, D.; Tyagi, A. K. Corundum Type Indium Oxide Nanostructures: Ambient Pressure Synthesis from InOOH, and Optical and Photocatalytic Properties. *RSC Adv.* **2016**, *6* (110), 108393–108403.
- (47) Kim, W. J.; Min, B.-K.; Pradhan, D.; Sohn, Y. Crystal Phase Transformation and Doping-Induced Blue Emission of Eu-Doped InOOH and Cubic/Corundum-Type Rhombohedral In₂O₃ Nanowires. *CrystEngComm* **2015**, *17* (5), 1189–1200.
- (48) Hu, Q.; Tan, R.; Li, J.; Song, W. Highly Conductive C12A7:E-Electride Nanoparticles as an Electron Donor Type Promoter to P2S

for Enhancing Photocatalytic Hydrogen Evolution. *J. Phys. Chem. Solids* **2021**, *149*, 109810.

(49) Giannakopoulou, T.; Papailias, I.; Todorova, N.; Boukos, N.; Liu, Y.; Yu, J.; Trapalis, C. Tailoring the Energy Band Gap and Edges' Potentials of g-C₃N₄/TiO₂ Composite Photocatalysts for NO_x Removal. *Chem. Eng. J.* **2017**, *310*, 571–580.

(50) Zhang, F.; Li, X.; Zhao, Q.; Chen, A. Facile and Controllable Modification of 3D In₂O₃ Microflowers with In₂S₃ Nanoflakes for Efficient Photocatalytic Degradation of Gaseous Ortho -Dichlorobenzene. *J. Phys. Chem. C* **2016**, *120* (34), 19113–19123.

(51) Braslavsky, S. E.; Braun, A. M.; Cassano, A. E.; Emeline, A. V.; Litter, M. I.; Palmisano, L.; Parmon, V. N.; Serpone, N. Glossary of Terms Used in Photocatalysis and Radiation Catalysis (IUPAC Recommendations 2011). *Pure Appl. Chem.* **2011**, *83*, 931.

(52) Zhang, G.; Sun, J.; Chen, D.; Li, N.; Xu, Q.; Li, H.; He, J.; Lu, J. Hierarchical Core-Shell Heterostructures of ZnIn₂S₄ Nanosheets on Electrospun In₂O₃ Nanofibers with Highly Enhanced Photocatalytic Activity. *J. Hazard. Mater.* **2020**, *398*, 122889.

(53) Zhang, X.; Liu, Y.; Ren, M.; Yang, G.; Qin, L.; Guo, Y.; Meng, J. Precise Carbon Doping Regulation of Porous Graphitic Carbon Nitride Nanosheets Enables Elevated Photocatalytic Oxidation Performance towards Emerging Organic Pollutants. *Chem. Eng. J.* **2022**, *433*, 134551.

(54) Chen, C.; Jiang, T.; Hou, J.; Zhang, T.; Zhang, G.; Zhang, Y.; Wang, X. Oxygen Vacancies Induced Narrow Band Gap of BiOCl for Efficient Visible-Light Catalytic Performance from Double Radicals. *J. Mater. Sci. Technol.* **2022**, *114*, 240–248.

(55) Jabeen, S.; Aadil, M.; Williams, J.; Awan, M. S.; Iqbal, J.; Zulfiqar, S.; Nazar, N. Synthesis of In₂O₃/GNPs Nanocomposites with Integrated Approaches to Tune Overall Performance of Electrochemical Devices. *Ceram. Int.* **2021**, *47* (16), 22345–22355.

(56) Sun, L.; He, X.; Zeng, S.; Yuan, Y.; Li, R.; Zhan, W.; Chen, J.; Wang, X.; Han, X. Double Insurance of Continuous Band Structure and N-C Layer Induced Prolonging of Carrier Lifetime to Enhance the Long-Wavelength Visible-Light Catalytic Activity of N-Doped In₂O₃. *Inorg. Chem.* **2021**, *60* (2), 1160–1171.

(57) Wang, Q.; Chen, Y.; Liu, X.; Li, L.; Du, L.; Tian, G. Sulfur Doped In₂O₃-CeO₂ Hollow Hexagonal Prisms with Carbon Coating for Efficient Photocatalytic CO₂ Reduction. *Chem. Eng. J.* **2021**, *421*, 129968.